An Integrated modeling and Observational Study of Three-Dimensional Upper Ocean Boundary Layer Dynamics and Parameterizations

Craig M. Lee, Eric A. D'Asaro, Ramsey Harcourt and Luc Rainville
Applied Physics Laboratory, University of Washington
1013 NE 40th St.
Seattle, WA 98105-6698
phone: (206) 685-7656 (Lee), (206) 685-2982 (D'Asaro), (206) 221-4662 (Harcourt)
fax: (206) 543-6785
email: craig@apl.washington.edu, dasaro@apl.washington.edu, harcourt@apl.washington.edu
Grant N00014-08-1-0445

Grants #'s: N00014-05-1-0329, N00014-05-1-0330, N00014-05-1-0331

http://opd.apl.washington.edu/~craig
http://opd.apl.washington.edu/~dasaro
http://opd.apl.washington.edu/~harcourt

LONG-TERM GOALS

This study contributes to our long-term efforts toward understanding:

- Mixed layer dynamics
- Processes that communicate atmospheric forcing to the ocean interior.

OBJECTIVES

Existing high resolution regional models typically resolve the mean vertical structure of the upper ocean boundary layer. Physically-based parameterizations of vertical fluxes make it possible to account for subgrid mixing at length scales smaller than the layer depth, but no specialized parameterization is used to represent the dynamics of horizontal mixing below the O(1)*km* - O(10)*km* resolution scale. We aim to determine the physical limitations of subgrid parameterization on these scales. This project addresses the following questions:

- What physics govern horizontal and vertical mixing in the presence of horizontal variability on the 1-10 km scale?
- What is the relative importance of horizontal and vertical mixing in determining the structure of the boundary layer?
- How well can existing parameterizations simulate vertical and horizontal mixing?
- What physics should be included to improve parameterizations?

APPROACH

An adaptive measurement program employed acoustically-tracked, neutrally buoyant Lagrangian floats and a towed, undulating profiler to investigate the relative importance of vertical and horizontal mixing in governing boundary layer structure in the presence of O(1 km) scale horizontal variability. Remotely sensed sea surface temperature and ocean color, combined with rapid, high-resolution towed surveys and model results guide float deployments to key locations within fronts. Synoptic, high-

resolution surveys followed Lagrangian float drifts to characterize three-dimensional variability within the span of a model grid points. Acoustic tracking allowed towed surveys to follow floats and geolocated all observational assets for later analysis. Measurements characterized boundary layer turbulence and facilitate detailed separation of vertical and horizontal processes.

A turbulence-resolving Large Eddy Simulation (LES) was used to model the dynamics of vertical and horizontal mixing in a domain volume corresponding to a regional model's horizontal gridscale and set in the translating Lagrangian reference frame of the float/survey observations. The observations will provide realistic initial and time-dependent boundary conditions and, in particular, time-dependent lateral boundary conditions will be determined from rapid surveys.

Quantitative one-to-one statistical comparisons between LES results and the float and survey observations will be made. This product will have direct application to assessing regional model subgrid parameterizations.

WORK COMPLETED

The 2006 Measurement Program: Observations in the California Current

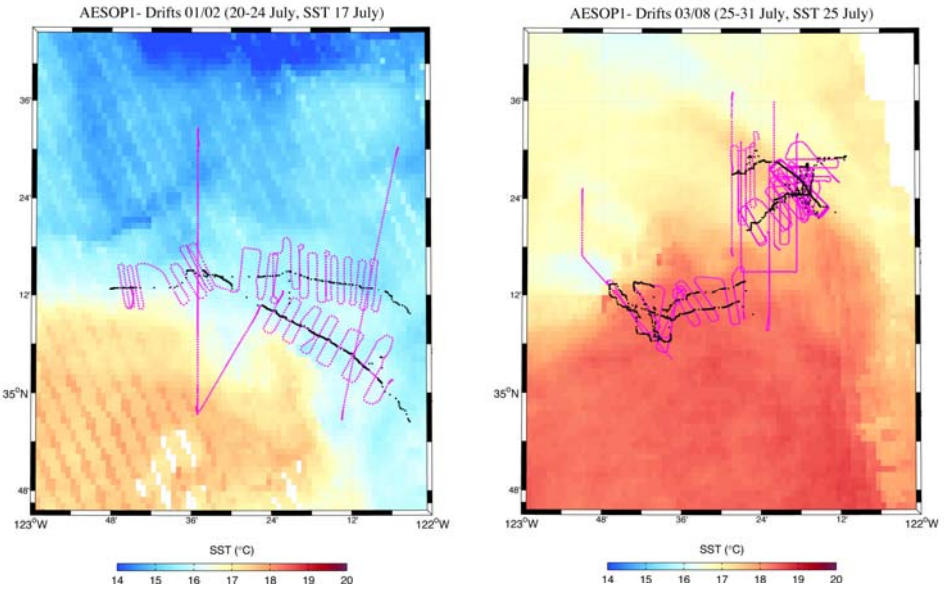

Figure 1. *Float drift (black) and towed profiler (magenta) tracks plotted over remotely sensed sea surface temperature. The bathymetry rises from the abyss near the eastern margin of the chart.*

The first of two cruises associated with this AESOP effort took place from R/V Roger Revelle, 16 July – 8 August 2006 off the California coast. Operations began with instrument testing and acoustic tracking refinement in the Channel Islands and Santa Barbara channel. Following this, two drifting surveys focused on a zonally oriented front located west of the continental rise off of San Luis Obispo (Fig. 1). A third drift followed the southward flow associated with a strong meridionally oriented front (Fig. 2). Sections occupied prior to float deployment exhibit T-S characteristics, small pycnostads and optical signatures that suggest active subduction of cold-side waters into the region below the warm-side mixed layer base (Fig. 2). Informed by float behavior inferred from model results analyzed before the cruise and by the high-resolution towed profiler section occupied immediately prior to float deployment, we selected a site intended to maximize the probability of observing subduction. Our first few deployments, during periods of weak wind, found little evidence for subduction driven by

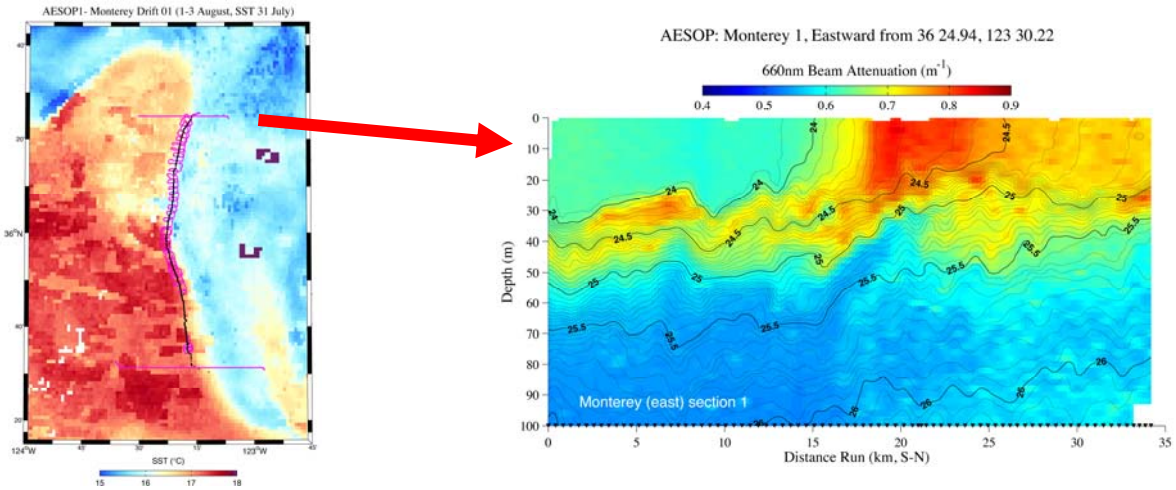

Figure 2. *(left) Front-following drift with line colors as defined in Fig. 1. (right) Potential density (contours) and 660 nm beam attenuation (colors) from the section used to choose the float deployment site.*

submesoscale processes alone. Our final two deployments, spanning a period of rising, sustained and then relaxing winds, clearly showed subduction and restratification as the front relaxed after the wind dropped.

The 2007 Measurement Program: Observations in the Kuroshio Extension

Building on lessons learned working off the California coast in 2006, the 2007 field effort focused on the strong fronts and submesoscale features associated with the Kuroshio extension. As during the previous cruise, near-realtime remotely sensed images and numerical results guided sampling to promising features. This resulted in three surveys, described below.

The first deployment (Fig. 3) was placed nearby in the Kuroshio extension third meander and focused on a meridionally-oriented section of front forced by southerly (up-front) winds. We anticipated, and found, that the upfront winds would drive frontalysis, spreading light, warm-side waters over denser cold-side waters. We hoped that blocking of Ekman transport by the fronts' relative vorticity field would cause downwelling. However, the front remained weak during the roughly four day survey with the float experiencing no downwelling events.

The second survey (Fig. 4) focused on a steep southward meander that NLOM forecasts predicted would detach within a few days time. Strong northerly winds provided frontogenic (downwind) forcing along the western side of the loop and frontolytic (upwind) forcing over the eastern side. The pre-deployment survey revealed strong fronts marking both sides of the feature, with the deepest mixed layers along the western margin. We deployed a float at the strongest gradient region of the front on the western side, calculating that it would transit over the 'U'-shaped path over 3-4 days contrasting the response to down-front and up-front wind forcing. Over four days of weakening winds, the fronts marking both sides of the meander became more diffuse, with a buoyant cap restratifying the mixed layer across the entire feature.

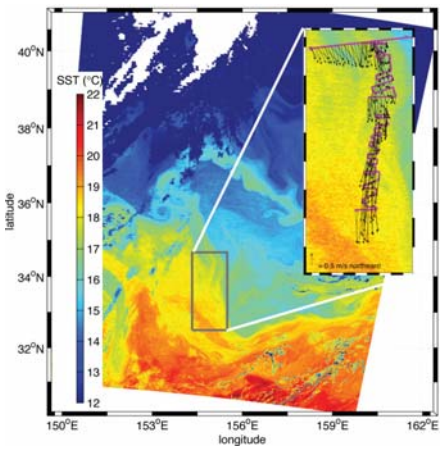

Figure 3. First Kuroshio survey. Colors show MODIS SST image. Inset shows the survey.

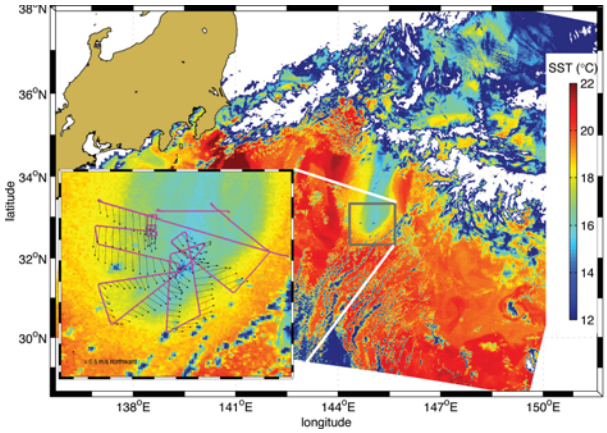

Figure 4. Second Kuroshio survey in a detaching meander – "The Sock"

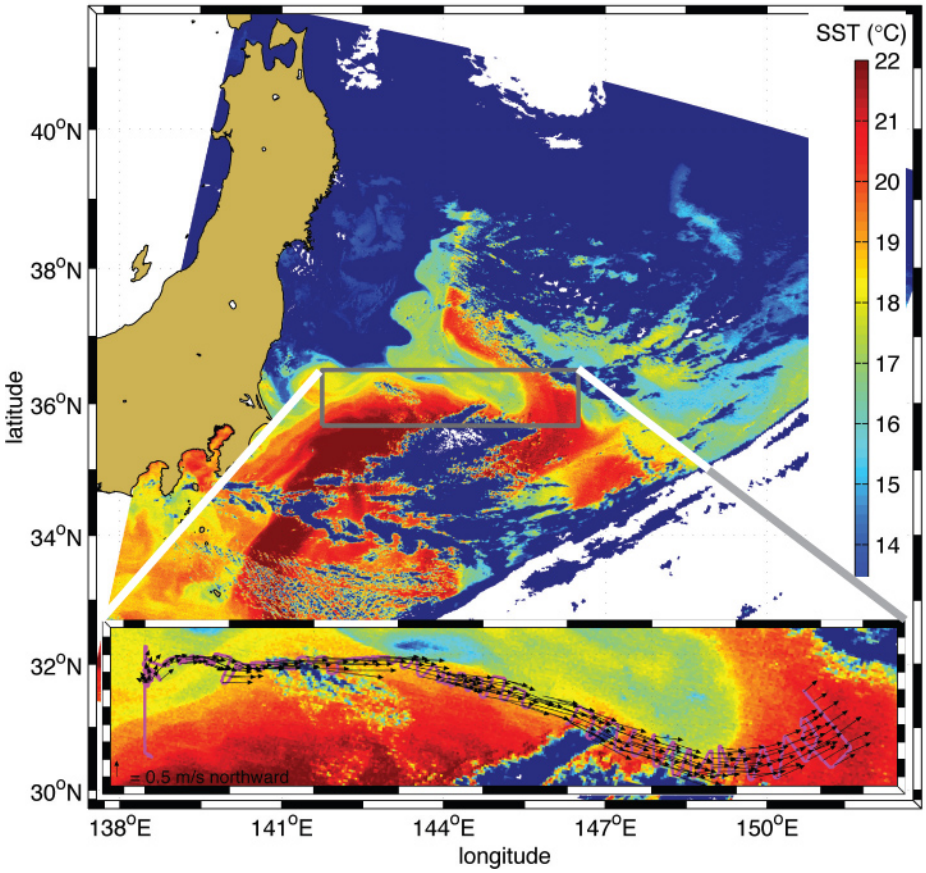

Figure 5. The third survey of the 2007 cruise, focusing on the first section of the Kuroshio extension. The survey (lower insert) followed the front as it is advected westward from its creation off the Japanese coast by the convergence of the cold Oyashio and warm Kuroshio currents.

The final survey focused on the strong, nearly linear , sharp and zonally-oriented section of Kuroshio front extending offshore from Japan (Fig. 5). Forcing by northwesterly (downfront) winds provided an ideal combination. The pre-deployment section revealed intense cyclonic relative vorticity and optical signals indicative of recent subduction in strong gradient region. Over a 7-day period, Triaxus repeatedly occupied cross-front sections following the drifting float, attempting to characterize a region marked by two outcropping isopycnals. Results from this survey are described in detail below.

Data Processing and Analysis

Triaxus towed profiler, float and shipboard data have been processed for both cruises. Triaxus-mounted ADCP data have been processed for both deployments. Analysis efforts have focused on restratification observed at a front in the California Current and on the evolution of a particularly sharp, wind-forced from in the Kuroshio. The Kuroshio analysis resulted in a paper published in Science, while the California Current analysis is still in progress. This work involves collaboration with Dr. Andrey Shcherbina (APL-UW) and Dr. Leif Thomas (Stanford).

RESULTS

Please see the attached paper, published in Science.

IMPACT/APPLICATION

None.

TRANSITIONS

None.

RELATED PROJECTS

SeaSoar and Doppler Sonar Spatial Survey of Internal Tide Generation and Mixing, Shaun Johnston and Daniel Rudnick.

Lagrangian Studies of Lateral Mixing (a component of the Lateral Mixing DRI). Craig Lee and Eric D'Asaro.

REFERENCES

Lee, C. M., L. N. Thomas and Y.Yoshikawa, 2006: Intermediate Water Formation at the Japan/East Sea Subpolar Front. *Oceanography*, 19(3), 54-64.

Thomas, L. and C. M. Lee, 2005: Intesification of Ocean Fronts by Down-front Winds. *Journal of Physical Oceanography*, 35(6), 1086-1102.

PUBLICATIONS

D'Asaro, E., C. Lee, L. Rainville, R. Harcourt and L. Thomas (2011). Enhanced Turbulence and Energy Dissipation at Ocean Fronts. *Science* 332(6027):318-322, doi: 10.1126/science.1201515.

Enhanced Turbulence and Energy Dissipation at Ocean Fronts

Eric D'Asaro, *et al.*

Science **332**, 318 (2011);
DOI: 10.1126/science.1201515

Enhanced Turbulence and Energy Dissipation at Ocean Fronts

Eric D'Asaro,[1]* Craig Lee,[1] Luc Rainville,[1] Ramsey Harcourt,[3] Leif Thomas[2]

The ocean surface boundary layer mediates air-sea exchange. In the classical paradigm and in current climate models, its turbulence is driven by atmospheric forcing. Observations at a 1-kilometer-wide front within the Kuroshio Current indicate that the rate of energy dissipation within the boundary layer is enhanced by one to two orders of magnitude, suggesting that the front, rather than the atmospheric forcing, supplied the energy for the turbulence. The data quantitatively support the hypothesis that winds aligned with the frontal velocity catalyzed a release of energy from the front to the turbulence. The resulting boundary layer is stratified in contrast to the classically well-mixed layer. These effects will be strongest at the intense fronts found in the Kuroshio Current, the Gulf Stream, and the Antarctic Circumpolar Current, all of which are key players in the climate system.

Although the basic characteristics of ocean circulation have been well known for many decades, a detailed understanding of its energetics has emerged only recently (*1*). The energy sources are well understood: Wind stress acting on surface currents (or "wind-work"), particularly in the Southern Ocean, is the dominant energy source, with little net input from heating/cooling or precipitation/evaporation. The energy sinks, however, are less well understood. Energy dissipation requires a cascade of energy through nine orders of magnitude, from the size of the ocean to the centimeter scales of viscous dissipation. A cascade of processes supports this flux. Instabilities of the large-scale circulation lead to the generation of a rich field of eddies with typical scales of 100 km at mid-latitudes. The dynamics of these eddies are highly constrained by Earth's rotation such that their currents are nearly geostrophic (that is, the flow is governed by a balance between Coriolis and horizontal pressure forces). A turbulent, geostrophic eddy field tends to flux energy to larger rather

[1]Applied Physics Laboratory and School of Oceanography, University of Washington, Seattle, WA 98105–6698, USA. [2]Department of Environmental Earth System Science, Stanford University, Palo Alto, CA 94305–4216, USA. [3]Applied Physics Laboratory, University of Washington, Seattle, WA 98105–6698, USA.

*To whom correspondence should be addressed. E-mail: dasaro@apl.washington.edu

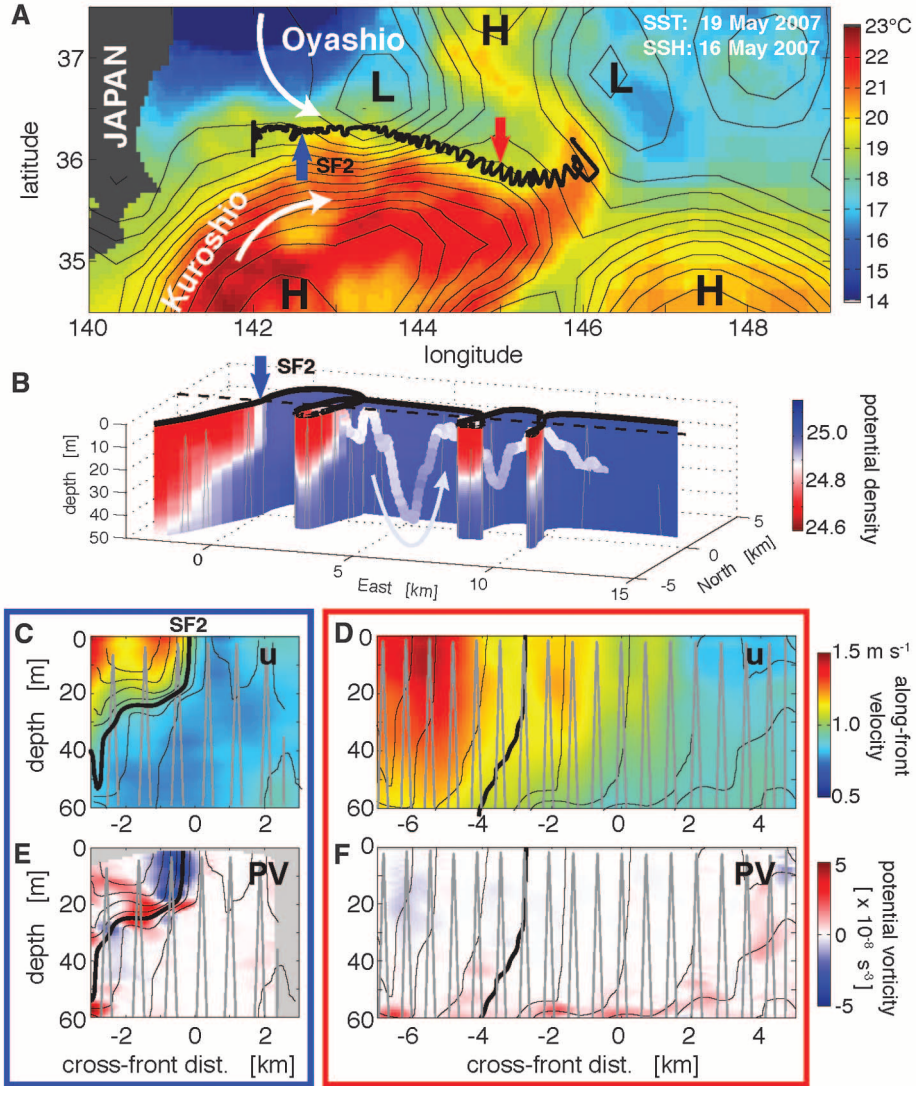

Fig. 1. (**A**) Sea surface temperature (SST) map (*37*) of experimental area with sea surface height (SSH) (*8*) shown as contours (0.1-m interval). The thick black line denotes the ship track. Blue and red arrows mark sections shown below in blue and red boxes (**C** to **F**), respectively. L and H mark low- and high-pressure centers, respectively. (**B**) Triaxus and float data around SF2 [blue box (C and E)], with Triaxus density shown as a colored curtain hanging beneath the ship track and float trajectory shown as a ribbon colored by density beneath the surface track (dashed line). Sections show along-front velocity [(C) and (D)] and total PV [(E) and (F)] for SF2 (left, blue box) and for a later section (right, red box). Black contours plot potential density in each section, with the thick line marking $\sigma_\theta = 25.0$ kg m^{-3} and thinner lines plotted at 0.05 intervals. Gray lines denote the Triaxus profile track.

than smaller scales, thus providing no obvious path to dissipation. Recent simulations (*2*–*4*) with very-high-resolution models suggest a new path from the eddy field toward dissipation through the formation of submesoscale fronts, regions of strong lateral gradient in the upper ocean, with horizontal scales of 1 to 10 km. Instabilities of these fronts could then cascade energy from the frontal scale to dissipation.

The simulations also suggest that the surface "mixed-layer" of the ocean is greatly modified in the presence of fronts. For one, the boundary layer is stratified, not mixed, and deepens by the action of turbulent motions that derive part of their energy from the frontal circulation as opposed to atmospheric forcing (*4*, *5*). This is a shift from the classical paradigm of a surface boundary layer driven by the atmosphere, with implications for climate dynamics. The surface boundary layer is the mediator for air-sea interaction and therefore influences processes that play an integral role in the climate system such as the oceanic sequestration of carbon and the subduction, or transfer, of heat, salt, and dissolved gasses from the ocean's surface to its interior. Oceanic sequestration of carbon and subduction occur to a large degree in the proximity of the ocean's main currents: the Gulf Stream, the Antarctic Circumpolar Current, and the Kuroshio Current (*6*, *7*). These currents are regions of strong lateral density gradients; therefore, their surface boundary layers could be substantially affected by frontal dynamics. Here, we present experimental evidence from a front in the Kuroshio showing that this is indeed the case.

Evolution of the front. Measurements were taken from 18 to 21 May 2007 (days 137 to 140) near the start of the Kuroshio extension off the coast of Japan. Here, the cold subpolar gyre waters of the Oyashio Current meet the warm subtropical gyre waters of the Kuroshio Current to form the Kuroshio front (Fig. 1A). The region is rich in eddies, as illustrated by the sea surface height contours in Fig. 1A (*8*). Measurements focused on an exceptionally sharp front [the "sharpest front" (SF), blue arrow in Fig. 1] formed by a strongly confluent flow between two eddies acting on the contrast between the warm Kuroshio water and the cold Oyashio water. Measurements were made by deploying a subsurface, neutrally buoyant Lagrangian (water-following) float (*9*) in the frontal region, acoustically tracking it from the ship, and surveying a ~5-km region around the float using the Triaxus profiling vehicle towed behind the *R/V Melville* (*10*). An example of the sampling strategy is shown in Fig. 1B. The float provided a reference frame moving with the frontal water, so that changes in frontal structure can be interpreted as attributable to its temporal evolution. The vertical motion of the float within the boundary layer also provided estimates of the turbulence intensity and dissipation rate. Measurements included temperature, salinity, and pressure on both platforms and velocity profiles obtained by combining ship and Triaxus data (fig. S3) (*10*).

Confluent flow (evident in Fig. 1A) concentrates the large-scale north-south temperature and salinity gradients into a smaller region, thus forming the SF. During day 137, estimates from the large-scale velocity field derived from satellite altimetry show a north-south convergence of north velocity $\partial v/\partial y < 0$ (v, northward velocity; y, northward distance) and an east-west divergence of east velocity $\partial u/\partial x > 0$ (u, eastward velocity; x, eastward distance), both of magnitude ~0.5×10^{-5} s^{-1}. Estimates from direct velocity measurements (fig. S3) (*10*) along the front and ±3 km to either side confirm the north-south convergence and the acceleration of the along-front velocity ($\partial u/\partial x \approx -\partial v/\partial y \sim 1.2 \pm 0.7 \times 10^{-5}$ s^{-1}). The observed front thinned laterally by about a factor of 2 during this period (Fig. 2A), a rate close to that predicted from these velocity gradients, thus forming and maintaining the SF through day 137. Both confluence components dropped to zero by day 138.5 and then become divergent with a magnitude of $0.5 \pm 0.5 \times 10^{-5}$ s^{-1}. Thus, the SF is a transient region of strong density gradient generated by strong local confluence and embedded within the larger-scale Kuroshio front.

A section across the SF (Fig. 1C) shows it to be less than 1 km wide in surface density and ~20 m deep (*11*). A surface-velocity maximum, the frontal jet, is found on the warm side of the front (Fig. 1C). The shear below this jet extends across the frontal region and has a substantial geostrophic component, but with a shear magnitude that is roughly half that expected geostrophically from the horizontal density gradient. A similar section taken 2 days and 220 km downstream (Fig. 1D) shows a much wider (4 km) and deeper (60 m) frontal zone. The large horizontal density gradients across the front have eroded, although the net contrast remains about the same, and the volume of water with intermediate properties has increased (Fig. 1, C and D). Thus, the decay of the SF appears to be due to a combination of local difluence and mixing.

Turbulence and mixing at the front. Measurements collected by the Lagrangian float at the SF quantify the rate of turbulent mixing. The float interspersed periods of Lagrangian drift with profiles and surfacing for communication. During the 16 drifts, the float was water-following in three dimensions, with its vertical velocity measuring the vertical velocity of the water. During

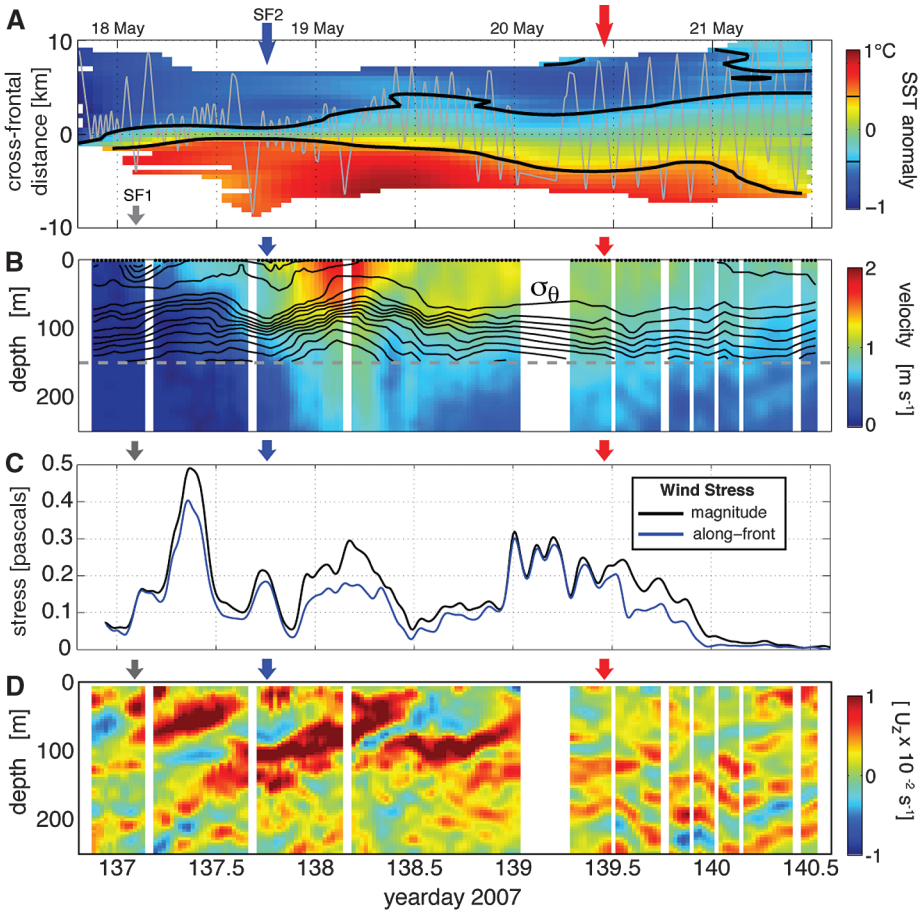

Fig. 2. (**A**) SST anomaly (relative to SST along the front) from ship surveys plotted relative to float position. Vertical axis is cross-frontal distance. (**B**) Depth-time section of along-front velocity following the float with potential density contoured at 0.2–kg m^{-3} intervals where available in the upper 150 m. (**C**) Wind stress (*22*, *23*) magnitude and along-front component in pascals. (**D**) Vertical shear (U_Z) of zonal velocity as a function of depth and time along the front.

profiles and surfacings, the float purposefully moved relative to the water and was thus not Lagrangian. The float sampled the SF during two of the drifts, which will hereafter be called SF1 and SF2. During these drifts, especially SF2, the float was exactly at the front, as indicated by: (i) its track (Fig. 1B), which follows the frontal interface mapped by the Triaxus; (ii) its density (Fig. 3B), which is intermediate between that of the warm and cold sides of the front; and (iii) its location at the maximum in horizontal density gradient (Figs. 1B and 3A). During these drifts, the float repeatedly cycles across the upper-ocean boundary layer (Fig. 3E), tracing the trajectories of boundary-layer water parcels and thus measuring their vertical velocity. Numerous other measurements in both convection (*12*, *13*) and wind-forced boundary layers (*14*–*17*) confirm that the vertical motion of these floats is due to upper-ocean turbulence.

What is the energy source for this turbulence? Numerous float observations of the average vertical kinetic energy (VKE) in the upper-ocean boundary layer show a remarkably good correlation between VKE and the 10-m wind speed (Fig. 3C). This correlation indicates that wind is usually the major source of energy for upper-ocean turbulence (*18*). However, the VKE during SF2 (gray in Fig. 3C) lies far (a factor 6) above these values, suggesting that wind cannot explain the anomalously high turbulence levels at SF2.

In Fig. 3D, the anomalously high turbulence at SF2 is shown in terms of energy dissipation rate; that is, the flux of energy through the turbulence. The average dissipation in the boundary layer is estimated from the frequency spectra of float vertical acceleration (Fig. 3D, black circles, and fig. S4) (*10*, *19*) and plotted as depth-integrated dissipation by multiplying by the boundary-layer depth (Fig. 3E) (*20*). Dissipation rate and energy are closely linked so that a second estimate with higher time resolution can be formed from the VKE (Fig. 3D, solid and dashed gray traces and open circles) (*21*). The average dissipation at SF2 rises by a factor of ~10 to 20 above the nonfrontal values with the VKE estimate suggesting that even higher values occurred just before the measurements began.

Cooling of the ocean by the atmosphere drives boundary-layer turbulence with an average dissipation rate given by the surface buoyancy flux (*12*). At SF2, very weak cooling occurs (*22*, *23*), with a buoyancy flux of less than 0.3% of the measured dissipation. Atmospheric cooling cannot explain the anomalously high turbulence levels at SF2.

In summary, SF2 is unremarkable in wind stress (Fig. 2C) or in velocity (Fig. 2B), but is highly anomalous in turbulence level (Fig. 3, C and D) and in lateral gradient (Fig. 2A).

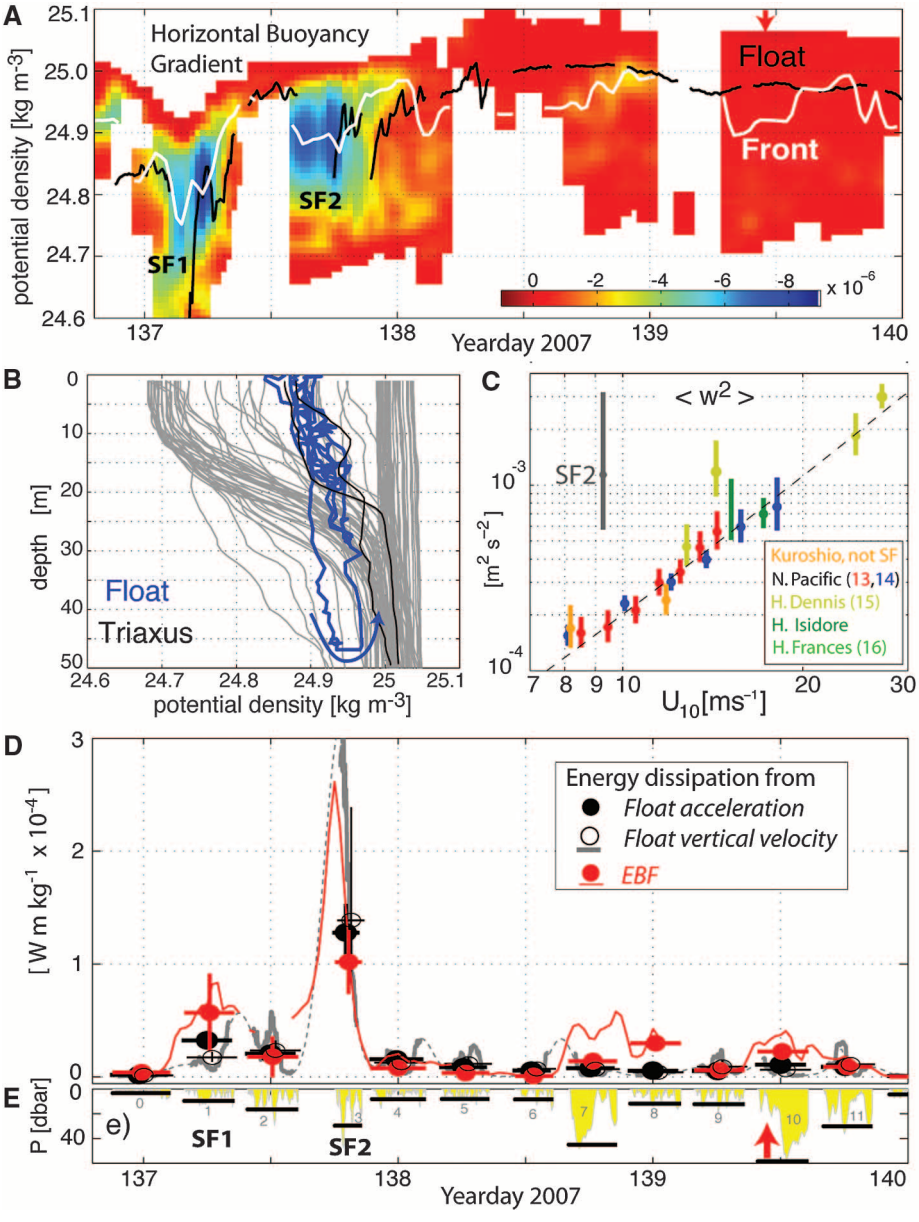

Fig. 3. (**A**) Horizontal buoyancy gradient, proportional to minus the density gradient (represented by color), computed from *R/V Melville*'s hull-mounted temperature sensor plotted as a function of time and potential density. The black line denotes the float trajectory, whereas the white line plots the position of maximum buoyancy gradient. (**B**) Density profiles at SF2 from float (blue) and Triaxus (gray) used in Fig. 1B. Two Triaxus profiles are highlighted (black). (**C**) Vertical velocity variance from floats (*14*–*17*) for wind-forced upper-ocean boundary layers as a function of wind speed. Confidence intervals (95%) were computed as in (*14*). SF2 lies well above all other data. U_{10}, the wind speed at 10-m height. (**D**) Time series of boundary-layer–integrated dissipation estimated from the float-acceleration spectrum (black solid circle), float VKE averaged over each float drift (open circles), 1-hour–averaged float VKE (gray line with dashed line interpolating between drifts), EBF computed at float averaged over drifts (red circles), and EBF computed at maximum density gradient (red line, 1.5-hours running average). (**E**) Float depth during Lagrangian drifts (yellow filled areas) and boundary-layer depth (black bars) estimated as twice the mean float depth.

Potential vorticity and frontal instability. We hypothesize that a flux of energy from the front itself accounts for the enhanced turbulence levels at SF2. The boundary layer at SF2 is stably stratified (Fig. 3B) yet highly sheared in the vertical direction due to the presence of a strong jet along the front (Fig. 2, B and C). This latter condition makes the flow potentially susceptible to symmetric instability (SI) (*4*), which extracts kinetic energy from the geostrophic frontal jet. The Ertel potential vorticity (PV) (*24*) is the key quantity for diagnosing this instability; a flow is unstable to SI when the PV is negative (*25*). PV can become negative due to the combination of a sufficiently strong vertical shear and lateral density gradient and a sufficiently weak vertical density gradient. These conditions can occur within the boundary layer of a strong front, with the front providing the shear and lateral gradient and the boundary layer having a reduced stratification. Simulations (*4*, *5*) indicate that under these conditions SI will grow, become unstable to secondary, smaller-scale instabilities (*26*), and feed a turbulent cascade to dissipation, resulting in a fully turbulent boundary layer drawing its energy from the front.

We used velocity and density data taken by the ship to evaluate the PV on each of the nearly 100 crossings of the front (fig. S5) (*10*, *24*). We found negative PV near the surface (Fig. 1E) for 0.2 days at SF2 and nowhere else (Fig. 1F). The front at SF2 is therefore unstable to SI, suggesting that the turbulence at SF2 is drawing energy from the frontal shear.

The simulations indicate that SI at a front occurs when the wind blows perpendicular to the frontal gradient (*27*, *28*), which is typically in the direction of the frontal velocity (Fig. 4). Such a "down-front" wind drives a net transport of water perpendicular to the frontal jet to carry heavy water across the front, from the cold side to the warm side. This Ekman transport advects heavy water over light water, reducing the stratification, and thus reducing the PV and promoting SI. The Ekman buoyancy flux (EBF) (*27*), computed from the product of the down-front wind stress (Fig. 2C) and the cross-frontal density gradient (Fig. 3A), is a measure of this effect. Simulations (*4*) suggest that turbulence in a fully developed boundary layer of depth H and driven by down-front winds extracts kinetic energy from the frontal jet at a depth-integrated rate given by $H(EBF)/2$ and dissipates it within the boundary layer. This quantity (*29*) peaks at SF2 (Fig. 3D, red) with a value comparable to the measured dissipation rate, thus providing quantitative evidence supporting the hypothesis that the boundary layer at SF2 was driven primarily by SI induced by a down-front wind.

The structure of the boundary layer also supports this hypothesis. SI acts to reduce the anomalously negative PV by inducing a circulation that increases the stratification, thereby counteracting the effect of the EBF (Fig. 4). Simulated boundary layers within symmetrically unstable fronts are simultaneously stratified and turbulent (*5*), in contrast to those outside of fronts, which are generally well mixed. Indeed, the observed density profiles within the front (Fig. 3B) lack mixed layers and are instead stratified at all depths. The Lagrangian float trajectories repeatedly cross this stratification, indicating that the boundary layer at SF2 is both turbulent and stratified (*30*).

Although SF1 exhibits elevated EBF and dissipation, the thin ($H \approx 10$ m) boundary layer precludes estimating PV and the towed surveys barely cross the front, making EBF errors large. An accurate evaluation of the hypothesis is not possible at SF1.

Near-inertial frequency waves. Sections of velocity and shear (Fig. 2, B and D) show that the above frontal processes are associated with deeper structures suggestive of internal waves. In particular, the depth-time section of shear (Fig. 2D) shows alternating diagonal stripes of positive and negative shear with upward phase propagation and a period close to the local inertial period (i.e., half a pendulum day: 0.84 days at this latitude). The north-south component of shear (not shown in Fig. 2) is in quadrature with the east-west component such that the velocity vector rotates clockwise with approximately constant magnitude as a function of both increasing depth and increasing time. This pattern is widely found in the ocean and interpreted as the signature of downward propagating near-inertial frequency internal waves (*31*). Given the observed stratification and estimating the vertical wavelength and period of the waves to be 200 m and 0.78 days, respectively (based on a least-squares fit on the shear field of the upper 150 m and first 2 days), theory predicts that the waves' downward energy flux is ~6 mW/m^2, which is similar to an estimate for the energy input to near-inertial waves from the winds of 9 mW/m^2 (*32*), but only about 6% of the excess turbulent dissipation at the SF2. These calculations suggest that the waves are probably driven by the winds and minimally contribute to the energetics of the turbulence within the boundary layer at the front.

Surprisingly, however, the strong near-surface shear of the sharpest front appears to be part of the deeper near-inertial pattern. The boundary-layer depth (Fig. 3E) also appears to have variability on roughly the same time scale; that is, the increased depth at days 138.7 and 139.6. Thus, it is possible that these inertial motions could play a role in the rapid confluence and difluence that generate and dissipate the SF, as well as in producing its negative PV. We further speculate that the SI at the front could feed energy into the inertial waves and thus radiate energy into the ocean interior. Because the lateral scale of the near-inertial motions is probably much larger than that of the SF, their overall role in the SF energetics could be substantially larger than that implied by the small local flux density.

Implications. Traditionally, the upper-ocean boundary layer is thought to be driven by the atmosphere through fluxes of heat, moisture, and momentum (*33*, *34*). The observations presented here break from this paradigm by suggesting that lateral density gradients and their geostrophic currents can also play a role in boundary-layer dynamics by supplying energy to turbulence at the expense of the circulation and permitting stratification and turbulence to coexist. Therefore, the greatly enhanced boundary-layer turbulence and dissipation described here in a very sharp Kuroshio front is likely an extreme example of a process that occurs much more widely in the ocean, potentially playing an important role in its dynamics

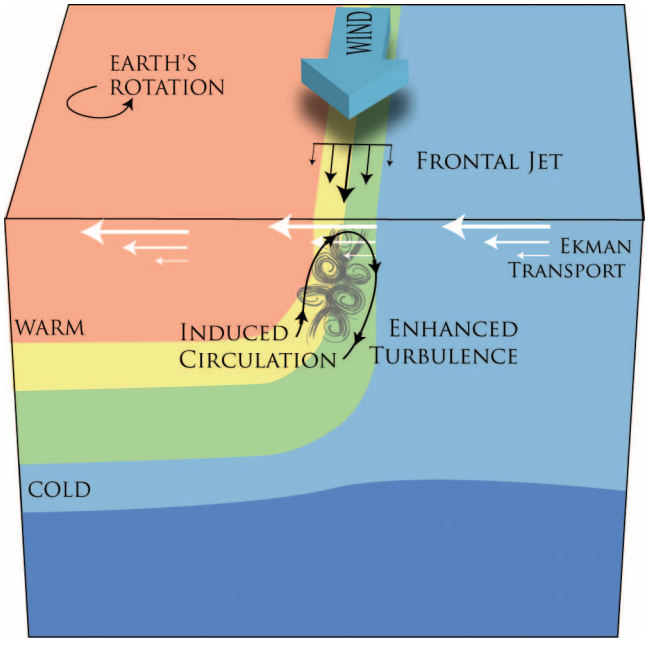

Fig. 4. Structure of the symmetrically unstable front. A wind blowing down the frontal boundary between warm and cold water induces an Ekman transport perpendicular to the wind and to the front. This carries heavy water from the cold side of the front over light water from the warm side, which, in the presence of the frontal jet and lateral density gradient, acts to reduce the stratification near the surface and makes the front unstable to symmetric instability. The instability draws energy from the frontal jet, leading to enhanced turbulence, and induces a circulation acting to bring warm water to the surface and cold water to depth, thus counteracting the effect of the Ekman transport and keeping the near-surface stably stratified, with warm water over cold water.

and energetics. Furthermore, these results are consistent with recent theory on submesoscale processes and thus encourage incorporation of this theory into boundary-layer models. Such physics is not accounted for in present-day climate models. Fronts associated with the Kuroshio, Gulf Stream, and Antarctic Circumpolar Current are key players in the ocean-atmosphere climate system. Inaccurate representation of the boundary layer and flow energetics in frontal regions could thus substantially affect the predictive skill of climate models.

References and Notes

1. R. Ferrari, C. Wunsch, *Annu. Rev. Fluid Mech.* **41**, 253 (2009).
2. X. Capet, J. C. McWilliams, M. J. Molemaker, A. F. Shchepetkin, *J. Phys. Oceanogr.* **38**, 2256 (2008).
3. J. Molemaker, J. C. McWilliams, X. Capet, *J. Fluid Mech.* **654**, 35 (2010).
4. L. N. Thomas, J. R. Taylor, *Geophys. Res. Lett.* **37**, L18606 (2010).
5. J. R. Taylor, R. Ferrari, *J. Phys. Oceanogr.* **40**, 1222 (2010).
6. C. L. Sabine *et al.*, *Science* **305**, 367 (2004).
7. D. Marshall, *J. Mar. Res.* **55**, 201 (1997).
8. The altimeter products were produced by Ssalto/Duacs (Segment Sol Multimissions d'Altimétrie, d'Orbitographie et de Localisation Précise/Data Unification and Altimeter Combination System) and distributed by Aviso (Archiving, Validation and Interpretation of Satellite Oceanographic Data), with support from the Centre National d'Etudes Spatiales (www.aviso.oceanobs.com/).
9. E. A. D'Asaro, *J. Atmos. Ocean. Technol.* **20**, 896 (2002).
10. See supporting online material for details of instrumentation and calculations.
11. Temperature measured continuously on the ship's hull shows a SF that is ~500 m wide, substantially smaller than the sampling scale of the Triaxus towed profiler. Triaxus data show a tight linear relation between potential temperature and potential density in the upper 10 m so that potential density can be accurately predicted from potential temperature (fig. S6A) (*10*).
12. E. L. Steffen, E. A. D'Asaro, *J. Phys. Oceanogr.* **32**, 475 (2002).
13. R. R. Harcourt, E. L. Steffen, R. W. Garwood, E. A. D'Asaro, *J. Phys. Oceanogr.* **32**, 493 (2002).
14. E. A. D'Asaro, *J. Phys. Oceanogr.* **31**, 3530 (2001).
15. R. Tseng, E. A. D'Asaro, *J. Phys. Oceanogr.* **34**, 1984 (2004).
16. E. A. D'Asaro, *J. Phys. Oceanogr.* **33**, 561 (2003).
17. E. A. D'Asaro, C. McNeil, *J. Mar. Syst.* **66**, 92 (2007).
18. For deep mixed layers, not shown in Fig. 3C, surface buoyancy flux can control the turbulence (*12*).
19. R.-C. Lien, E. D'Asaro, G. Dairiki, *J. Fluid Mech.* **362**, 177 (1998).
20. Boundary layer depth is computed as twice the mean depth of the float. This will be exactly true for a float whose depth is uniformly distributed across the boundary layer.
21. The kinetic energy in the boundary layer will be ~$1.5H\langle w^2\rangle$, where H is the boundary-layer depth, w is vertical velocity, and isotropic turbulence is assumed. This energy will dissipate in an eddy overturning time at approximately $H/\langle w^2\rangle^{1/2}$, thus predicting a depth-integrated dissipation rate of $1.5\langle w^2\rangle^{1.5}$. Figure 3D shows a plot of $3\langle w^2\rangle^{1.5}$. The constant 3 was chosen to best fit the dissipation estimates from acceleration. The difference could easily be due to the expected anisotropy of the boundary-layer turbulence and exact overturning time. The constant could vary with the boundary-layer dynamics; this analysis does not account for this possibility.
22. We computed surface fluxes of momentum, heat, and buoyancy from the IMET, Improved Meteorology measurements on the *R/V Melville* using the TOGA/COARE algorithms as implemented in the MATLAB air-sea toolbox (*23*). This results in estimates of the wind stress $\tau = \rho u_*^2$ (where ρ is air density, and u_* is the friction velocity) and the buoyancy flux J_b.
23. C. W. Fairall, E. F. Bradley, D. P. Rogers, J. B. Edson, G. S. Young, *J. Geophys. Res.* **101**, 3747 (1996).
24. The Ertel PV is defined as $Q = \omega_a \cdot \nabla b$, the dot product of the absolute vorticity $\omega_a = f\hat{k} + \vec{\zeta}$ and the gradient of buoyancy $b = -g\rho/\rho_0$. The coordinates are (x, y, z) for the along-front (east), cross-front (north), and up directions with associated velocity components (u, v, w). The Coriolis parameter is f, gravity's acceleration is g, potential density is ρ, ρ_0 is a reference density, and $\vec{\zeta}$ is the relative vorticity $\nabla \times \vec{u}$. Computationally, the vertical vorticity is estimated as $\zeta_z = -\partial u/\partial y$ and the cross-front component of vorticity as $\zeta_y = \partial u/\partial z$. The PV can be split into two parts: $Q = Q_V + Q_H$, where $Q_V = (f - \partial u/\partial y)\partial b/\partial z$ and $Q_H = (\partial u/\partial z)\partial b/\partial y$. A geostrophic flow is symmetrically unstable when its PV is negative and $Q_V > 0$.
25. T. W. N. Haine, J. Marshall, *J. Phys. Oceanogr.* **28**, 634 (1998).
26. J. R. Taylor, R. Ferrari, *J. Fluid Mech.* **622**, 103 (2009).
27. More accurately, down-front winds are defined as winds that induce a positive wind-driven buoyancy flux: $EBF = \rho_0^{-1}\vec{\tau}_w \cdot \partial\vec{u}_g/\partial z$, where $\vec{\tau}_w$ is the wind stress and $\partial\vec{u}_g/\partial z = f^{-1}\hat{k} \times \nabla b$ is the geostrophic shear. Thus, down-front winds have a component along the geostrophic shear.
28. L. N. Thomas, *J. Phys. Oceanogr.* **35**, 2457 (2005).
29. EBF and its statistical error are computed using a density gradient derived from temperature measured on the ship's hull (figs. S6 and S7) (*10*). Error estimates are dominated by the variance of the temperature observations on either side of the front, the uncertainty in the float position, and the uncertainty of the wind direction.
30. Three different measures of stratification—(i) the vertical density gradient measured from the Triaxus profiles (gray in Fig. 3B), (ii) the vertical density gradient from the float trajectories (blue in Fig. 3B), and (iii) the mean difference between CTDs on the top and bottom of the float (not shown in Fig. 3)—all indicate that the stratification is stable. Comparison of the two highlighted Triaxus profiles (black in Fig. 3B) with the float profile shows that although the deeper parts of the float profile differ from the mean Triaxus profile, some Triaxus profiles have a similar structure to that seen by the float.
31. K. D. Leaman, T. B. Sanford, *J. Geophys. Res.* **80**, 1975 (1975).
32. A simple slab model (*35*) with no damping and a 25-m-deep layer gains inertial energy at a rate of ~9 mW/m^2 between days 135.5 and 137.5, mostly due to wind bursts near days 136.3 and 137.3. This is sufficient to drive the observed near-inertial energy flux, although the complexities of near-inertial wave generation and propagation in a frontal region such as this (*36*) make a more exact analysis difficult to conduct.
33. Velocity differences across the bottom of the mixed layer also play an important role, but these are mostly driven by local winds (*34*).
34. J. F. Price, R. A. Weller, R. Pinkel, *J. Geophys. Res.* **91**, 8411 (1986).
35. E. A. D'Asaro, *J. Phys. Oceanogr.* **15**, 1043 (1985).
36. E. Kunze, *J. Phys. Oceanogr.* **15**, 544 (1985).
37. New Generation Sea Surface Temperature Development Group, Tohoku University, Sendai, Japan; www.ocean.caos.tohoku.ac.jp/.

Acknowledgments: This work was supported by the Office of Naval Research as part of the Assessing the Effects of Submesoscale Ocean Parameterizations program (grants N00014-05-1-0329/30/31, N00014-08-1-0445/10446/10447, and N00014-09-1-0202). This work would not have been possible without the efforts of staff at the Integrated Observations Group, the Ocean Engineering Department at the University of Washington Applied Physics Laboratory, and the crew and officers of the *R/V Melville*.

Supporting Online Material

www.sciencemag.org/cgi/content/full/science.1201515/DC1
SOM Text
Figs. S1 to S7
References

10 December 2010; accepted 1 March 2011
Published online 10 March 2011;
10.1126/science.1201515

Structure of an Agonist-Bound Human A_{2A} Adenosine Receptor

Fei Xu,[1] Huixian Wu,[1] Vsevolod Katritch,[2] Gye Won Han,[1] Kenneth A. Jacobson,[3] Zhan-Guo Gao,[3] Vadim Cherezov,[1] Raymond C. Stevens[1]*

Activation of G protein–coupled receptors upon agonist binding is a critical step in the signaling cascade for this family of cell surface proteins. We report the crystal structure of the A_{2A} adenosine receptor (A_{2A}AR) bound to an agonist UK-432097 at 2.7 angstrom resolution. Relative to inactive, antagonist-bound A_{2A}AR, the agonist-bound structure displays an outward tilt and rotation of the cytoplasmic half of helix VI, a movement of helix V, and an axial shift of helix III, resembling the changes associated with the active-state opsin structure. Additionally, a seesaw movement of helix VII and a shift of extracellular loop 3 are likely specific to A_{2A}AR and its ligand. The results define the molecule UK-432097 as a "conformationally selective agonist" capable of receptor stabilization in a specific active-state configuration.

G protein–coupled receptors (GPCRs) are critical cellular signal transduction gatekeepers for eukaryotic organisms. Some GPCRs are activated by ligands that act as agonists; others are inactivated by inverse agonists and antagonists. Efforts to elucidate the crystal structures of GPCRs bound to diffusible ligands have recently yielded structures for five class A (rhodopsin-like) GPCRs: the β_2 (*1*–*7*) and β_1 (*8*, *9*) adrenergic receptors (β_2AR and β_1AR), the A_{2A} adenosine receptor (A_{2A}AR) (*10*), the CXCR4 chemokine receptor (*11*), and the D3 dopamine receptor (*12*). All of these structures display a common seven-transmembrane (7TM) topology for GPCRs, as well as substantial variations in functionally divergent regions—especially on the extracellular side of the receptor, which is responsible for the recognition of a vast variety of

[1]Department of Molecular Biology, Scripps Research Institute, 10550 North Torrey Pines Road, La Jolla, CA 92037, USA. [2]Skaggs School of Pharmacy and Pharmaceutical Sciences and San Diego Supercomputer Center, University of California, San Diego, La Jolla, CA 92093, USA. [3]Laboratory of Bioorganic Chemistry, National Institute of Diabetes and Digestive and Kidney Diseases, Bethesda, MD 20892, USA.

*To whom correspondence should be addressed. E-mail: stevens@scripps.edu

REPORT DOCUMENTATION PAGE

Form Approved
OMB No. 0704-0188

1. REPORT DATE *(DD-MM-YYYY)*	2. REPORT TYPE	3. DATES COVERED *(From - To)*
04/26/2012	Final Report	2 February 2008 - 31 December 201

4. TITLE AND SUBTITLE
An Integrated modeling and Observational Study of Three-Dimensional Upper Ocean Boundary Layer Dynamics and Parameterizations

5a. CONTRACT NUMBER

5b. GRANT NUMBER
N00014-08-1-0445

5c. PROGRAM ELEMENT NUMBER

6. AUTHOR(S)
Craig M. Lee; Eric A. D'Asaro; Ramsey Harcourt and Luc Rainville.

5d. PROJECT NUMBER

5e. TASK NUMBER

5f. WORK UNIT NUMBER

7. PERFORMING ORGANIZATION NAME(S) AND ADDRESS(ES)
Applied Physics Laboratory
University of Washington
1014 NE 40th Street
Seattle, WA 98105

8. PERFORMING ORGANIZATION REPORT NUMBER

9. SPONSORING/MONITORING AGENCY NAME(S) AND ADDRESS(ES)
Scott L. Harper, Code ONR 322
Office of Naval Research
875 North Randolph Street
Arlington, VA 22203-1995

10. SPONSOR/MONITOR'S ACRONYM(S)

11. SPONSOR/MONITOR'S REPORT NUMBER(S)

12. DISTRIBUTION/AVAILABILITY STATEMENT
Approved for public release; distribution is unlimited.

13. SUPPLEMENTARY NOTES

14. ABSTRACT
Existing high resolution regional models typically resolve the mean vertical structure of the upper ocean boundary layer. Physically-based parameterizations of vertical fluxes make it possible to account for subgrid mixing at length scales smaller than the layer depth, but no specialized parameterization is used to represent the dynamics of horizontal mixing below the O(1)km - O(10)km resolution scale. We aim to determine the physical limitations of subgrid parameterization on these scales.

15. SUBJECT TERMS

16. SECURITY CLASSIFICATION OF:			17. LIMITATION OF ABSTRACT	18. NUMBER OF PAGES	19a. NAME OF RESPONSIBLE PERSON
a. REPORT	b. ABSTRACT	c. THIS PAGE			Craig M. Lee
U	U	U	UU	11	19b. TELEPHONE NUMBER *(Include area code)* (206) 543-4856